Letter | Editors' Suggestion

Reconfigurable topological modes in acoustic non-Hermitian crystals

Haiyan Fan,[1,2] He Gao,[1,*] Tuo Liu,[3] Shuowei An,[1] Xianghong Kong,[2] Guoqiang Xu,[2] Jie Zhu,[4,5] Cheng-Wei Qiu,[2,†] and Zhongqing Su[1,‡]

[1]*Department of Mechanical Engineering, The Hong Kong Polytechnic University, Hung Hom, Kowloon, Hong Kong SAR, China*
[2]*Department of Electrical and Computer Engineering, National University of Singapore, Singapore 116083, Singapore*
[3]*Key Laboratory of Noise and Vibration Research, Institute of Acoustics, Chinese Academy of Sciences, Beijing 100190, China*
[4]*Institute of Acoustics, School of Physics Science and Engineering, Tongji University, Shanghai 200092, China*
[5]*Shanghai Research Institute for Intelligent Autonomous Systems, Tongji University, Shanghai 201210, China*

(Received 3 January 2023; revised 22 March 2023; accepted 22 March 2023; published 9 May 2023)

Non-Hermiticity, usually represented in the context of gain and loss, gives rise to many exotic topological phenomena and offers more opportunities to steering topological functions. In modern acoustics, it has been widely perceived that the topological mode will be altered if topological phase changes. Our work shows otherwise in non-Hermitian acoustic crystals. We experimentally demonstrate an acoustic quadrupole topological insulator, whose topological corner, edge, and bulk modes could be arbitrarily engineered at any desired positions with its topological phase maintained. These non-Hermiticity-controlled topological modes bestow a bulk structure with unique features beyond the classical bulky state, offering a reconfigurable and versatile approach to manipulating topological phenomena. This non-Hermitian scheme can be readily generalized to other topological systems in various dimensions, such as the three-dimensional photonic/phononic lattices, which offer advanced and externally controllable recipes for manipulating topological phenomena.

DOI: 10.1103/PhysRevB.107.L201108

I. INTRODUCTION

The fascinatingly robust topological phenomena, such as the localized zero-dimensional high-density states in one-dimensional (1D) topological insulators, the 1D pathways in the two-dimensional (2D) spin/valley Hall insulators, and 2D surface transport in three-dimensional (3D) topological insulators [1–3] are typical topological bulk-boundary correspondences [4] with quantized dipole moments [5]. In addition, topological insulators can host quadrupole moments with energy localizations at the corners or hinges [6–8], which were experimentally demonstrated in versatile platforms, ranging from elastic wave [9], microwave [10], topolectrical-circuit [11], optical wave [12], to airborne acoustic wave [13]. Although the quadrupole topological insulators (QTIs) provide a solid foundation to effectively guide and localize energy, their flexible reconfigurability remains a challenge. For example, the topological corner states can only penetrate the bulk structure by introducing sufficient perturbations to induce a topological phase transition in the interior [14–16]. In fact, the indispensable bulk sites, which occupy an overwhelmingly large proportion of the entire structure, are not directly involved in transportation or localization [17]. Therefore, the development of desired topological devices toward miniaturization and integration is restricted. Here, we present a non-Hermitian approach to this issue.

Non-Hermiticity, arising from loss/gain or nonreciprocity, enables much richer topological phenomena, including the non-Hermitian skin effect with unconventional bulk-boundary correspondences [18–20], and non-Hermiticity-controlled topological phase transitions [21–25]. In addition, the non-Hermitian operators may give rise to the coalescence of two or more eigenvalues, known as exceptional points (EPs) [26,27], which leads to intriguing phenomena such as loss-induced lasing [28], unidirectional invisibility [29], and unidirectional sound focusing [30]. Recently, it was demonstrated that when the non-Hermitian parameter crosses the EP, the topological interface states can propagate along arbitrary gain and loss domain walls in a 2D photonic lattice [31]. Moreover, non-Hermiticity shows the capabilities to flexibly control the higher-order topological states at domain walls with arbitrary shapes [32]. But, how to experimentally realize the reconfigurable higher-order topological modes (TMs) remains unexplored.

In this paper, we experimentally demonstrate the flexible control of topological interface pathways and corner localizations in an acoustic QTI with the assistance of non-Hermiticity. The non-Hermitian modulation is implemented by introducing additional loss to a particular portion of the lattice [colored in blue in Fig. 1, termed as high-loss subarea (HLS)], while keeping the other sites intact [colored in red in Fig. 1, termed as low-loss subarea (LLS)]. Multiple TMs emerge at the interfaces of the HLS and LLS when the loss contrast exceeds the EPs, which contributes to guiding or localizing energy without changing the global topological phase of the lattice. Hence, the non-Hermiticity can serve as a key ingredient to control the TMs on demand by designing

*h.e.gao@connect.polyu.hk
†chengwei.qiu@nus.edu.sg
‡zhongqing.su@polyu.edu.hk

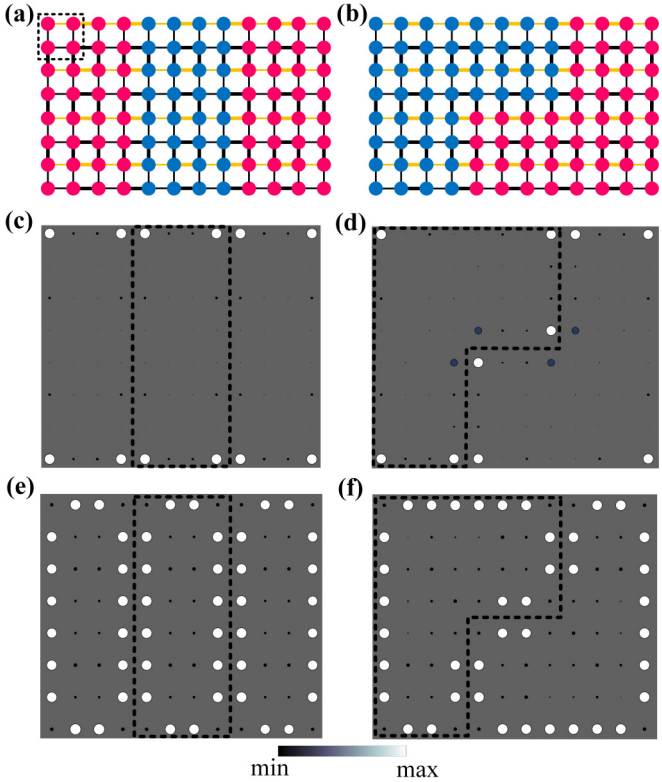

FIG. 1. Non-Hermitian modulation of the topological modes in a quadrupole topological insulator. (a), (b) Schematics of the QTI with the imbalanced loss distributions. Sites colored in blue (red) have high loss (low loss). Connecting lines colored in orange (black) represent positive (negative) hopping. The dotted black box marks one basic unit cell. (c), (d) Topological corner-mode profiles for the tight-binding models illustrated in (a) and (b), respectively. (e), (f) Topological edge-mode profiles for the tight-binding models illustrated in (a) and (b), respectively. In (c)–(f), the areas inside the dotted black boxes possess additional losses. Both the size and the color of the dots in (c)–(f) represent the intensity.

different patterns of the HLSs (Fig. 1), making the bulk sites useful.

II. THEORY

We start with the tight-binding model (TBM) for a QTI that supports a topological nontrivial band gap, where the intracell hopping is smaller than the intercell hopping. The orange and black connecting lines in Figs. 1(a) and 1(b) denote the positive and negative hoppings, respectively. In this QTI, the interior bulk sites are insulating, whereas the edge-transport pathways and corner localizations are topologically protected. If we uniformly add loss to all the sites of this QTI, still no in-gap states appear in the bulk as the uniform loss will not change its topological properties [31,33]. However, when two different losses are applied to the red and blue sites in Figs. 1(a) and 1(b), respectively, topological corner [Figs. 1(c) and 1(d)] and edge modes [Figs. 1(e) and 1(f)] will emerge along the interfaces with different loss areas. Both topological edge and corner modes can be flexibly relocated in various interfaces simply by tailoring the HLS pattern.

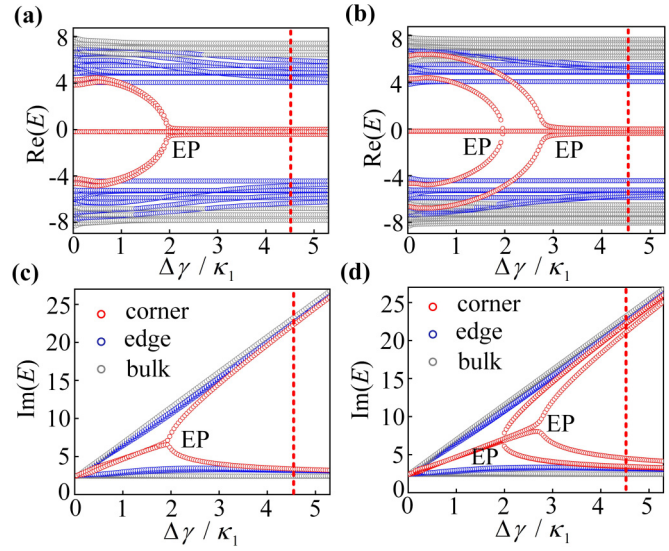

FIG. 2. Evolution of the eigenfrequency versus the loss contrast. (a), (b) Calculated real parts of the complex eigenvalues for the lattice illustrated in Fig. 1(a) and Fig. 1(b), respectively. (c), (d) Calculated imaginary parts of the complex eigenvalues for the lattice illustrated in Fig. 1(a) and Fig. 1(b), respectively. Red, blue, and gray circles, respectively, represent the eigenvalue evolution of corner, edge, and bulk modes as a function of the loss contrast ($\Delta\gamma = \gamma_2 - \gamma_1$). Red dashed lines denote the value used in the following measurements. In all calculations, the loss coefficient $\gamma_1 = 2.4$, the intracell coupling strength $\varepsilon_1 = 1$, and intercell coupling strength $\kappa_1 = 4.56$.

The imbalanced energy dissipation along the interface breaks the insulating interior, generating internal topological modes. The loss contrast $\Delta\gamma = \gamma_2 - \gamma_1$ (γ_1 and γ_2 are the loss coefficients in the LLS and HLS, respectively) is the key factor, which is evidenced by the calculated results based on the TBM, as shown in Fig. 2. When $\Delta\gamma = 0$, the finite-sized lattice is a standard QTI with corner modes pinned at the zero energy, and gapped edge and bulk modes distributed symmetrically about the zero energy. With the growth of the loss contrast, more corner (red circles in Fig. 2) and edge (blue circles in Fig. 2) modes emerge from the original edge and/or bulk regions. For the lattice configuration in Fig. 1(a), corner modes evolve from the two branches of edge modes [Fig. 2(a)] and coalesce to an EP (see note S1 in the Supplemental Material [33]) at $\Delta\gamma/\kappa_1 = 2$. Meanwhile, the edge modes, originating from the gapped bulk modes, gradually merge into the existing edge states as the loss contrast increases.

Furthermore, by reshaping the loss configurations as presented in Fig. 1(b), the loss-induced corner modes reside not only at the edges but also in the bulk sites [see Fig. 1(d)]. As a result, two pairs of corner modes originate from the edge and bulk modes and coalesce at $\Delta\gamma/\kappa_1 = 2$ and $\Delta\gamma/\kappa_1 = 2.8$, respectively, forming two EPs as presented in Figs. 2(b) and 2(d). After crossing the EPs, they share the same real part of eigenenergy but different imaginary parts. The modes with lower imaginary parts mainly locate in the LLS, while those with higher imaginary parts reside in the HLS, which confirms that they decouple with each other, and become topologically protected corner modes with robustness against various defects (see note S2 in Ref. [33]).

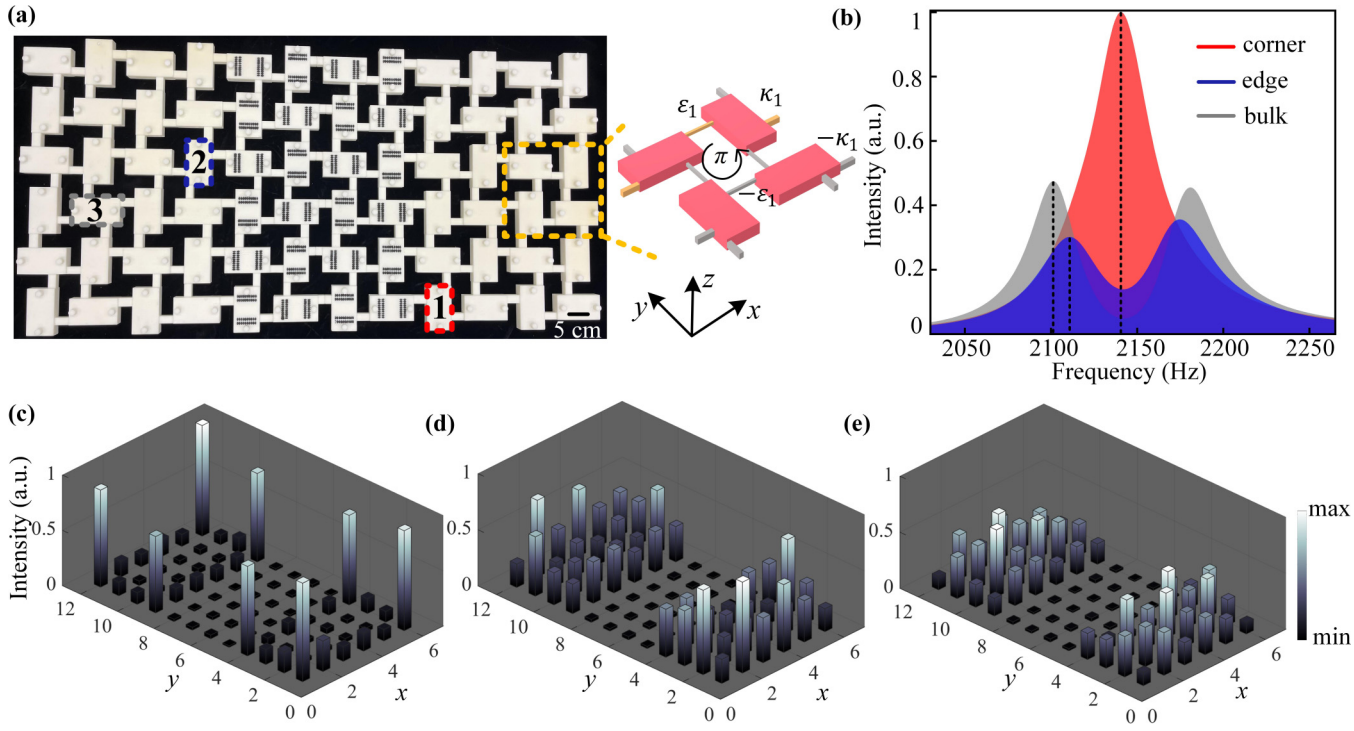

FIG. 3. Measured acoustic responses of the lattice with a rectangular HLS. (a) Photo of a sample with 6 × 12 site cavities. Inset illustrates one unit cell of the lattice. Length, width, and height of the cuboid cavities are 80, 40, and 10 mm, respectively. Coupling thin tubes have the same length of 40 mm, while the cross-sectional areas are 2.5 × 2.5 mm^2 for the intracell tubes ($\pm\varepsilon_1$) and 5 × 5 mm^2 for the intercell tubes ($\pm\kappa_1$). (b) Response spectra measured at cavities 1, 2, and 3 labeled in (a), corresponding to the edge-evolved corner (in red), bulk-evolved edge (in blue), and bulk (in gray) modes, respectively. (c)–(e) Measured acoustic intensity profiles at 2141, 2114, and 2100 Hz around the peaks of the corner, edge, and bulk spectra, respectively, indicated by the dashed black lines in (b). Not only the height but also the color of the bar can represent the intensity.

III. EXPERIMENT

We use coupled resonant cavities to experimentally implement the above TBMs [13,34–36]. Each unit cell in the designed acoustic QTI contains four cuboid acoustic cavities linked through thin tubes [inset in Fig. 3(a)]. Its quantized bulk quadrupole moment can be described by the quantized edge polarization $p_x^{v_y^{+(-)}} = p_y^{v_x^{+(-)}} = 0.5$ (see note S3 in Ref. [33]), following the nested Wilson-loop approach [7]. The sign of hopping can be directly adjusted by changing the location of the linking tube, without affecting the hopping amplitudes [37,38]. The intracell and intercell hopping strengths are $\varepsilon_1 = -5.5$ Hz and $\kappa_1 = -25.6$ Hz, respectively (for details see note S3 in Ref. [33]). For a single cavity, its resonant frequency and intrinsic loss are $f_0 = 2141$ Hz and $\gamma_1 = 0.0062$, respectively. By perforating the cavities with small leaky holes (the radius is 1.2 mm) and then inserting sound-absorptive materials [21,38], the additional loss $\Delta\gamma = \gamma_2 - \gamma_1$ ($\gamma_2 = 0.060$) is introduced (details are given in note S4 of Ref. [33]). Here, $\Delta\gamma/\kappa_1 = 4.5$, denoted by the red dashed line in Fig. 2, is sufficiently enough to exceed the EPs and separate the corner, edge, and bulk modes.

A rectangular acoustic lattice with coupled 6 × 12 cavities [Fig. 3(a)] is fabricated by stereolithography 3D printing to experimentally produce topological corner and edge modes, as predicted by the above calculations. For the sample in Fig. 3(a), the middle region (consisting of 6 × 4 cuboid cavities) is added with additional loss, which corresponds to the TBM in Fig. 1(a). Small pieces of sound-absorbing sponge (black) are inserted into the leaky holes of these cavities to compensate the frequency shift brought by the additional loss [21,38]. Each site cavity is drilled with two identical holes on the upper and lower sides (the radius is 1 mm) for inputting and measuring the sound signals. Without measurements, the holes are sealed by the matched cover lids [round protrusions in Fig. 3(a)]. In the experiment, the exciting signal and measuring microphone are located at the same cavity, and this process is repeated for all the cavities (see note S7 in Ref. [33] for more experimental details). The non-Hermiticity-enabled TMs distributed in the LLS dominate that in the HLS because they possess approximately the same quality factors as the original TMs (around 71; see Fig. S5 in Ref. [33]), whereas for the TMs in the HLS, the quality factor are very small (around 9). Therefore, the measured acoustic intensity spectra for cavities in the HLS are very low in amplitudes, and the intensity spectra for cavities in the LLS that we focused on are sufficiently high to characterize the TMs and the band gap.

We first probe the bulk band-gap property, so that a bulk cavity marked as "3" in Fig. 3(a) is excited and measured. Its response spectrum [the gray plot in Fig. 3(b)] has two peaks at 2100 and 2181 Hz, which correspond to the two branches of bulk modes with lower imaginary parts around 14 Hz (see Fig. S5(a) in Ref. [33]). Then, we measure a bulk cavity located in the middle of the interface with different losses [marked as "2" in Fig. 3(a)], where the formed edge modes are expected to emerge. The two peaks in the measured

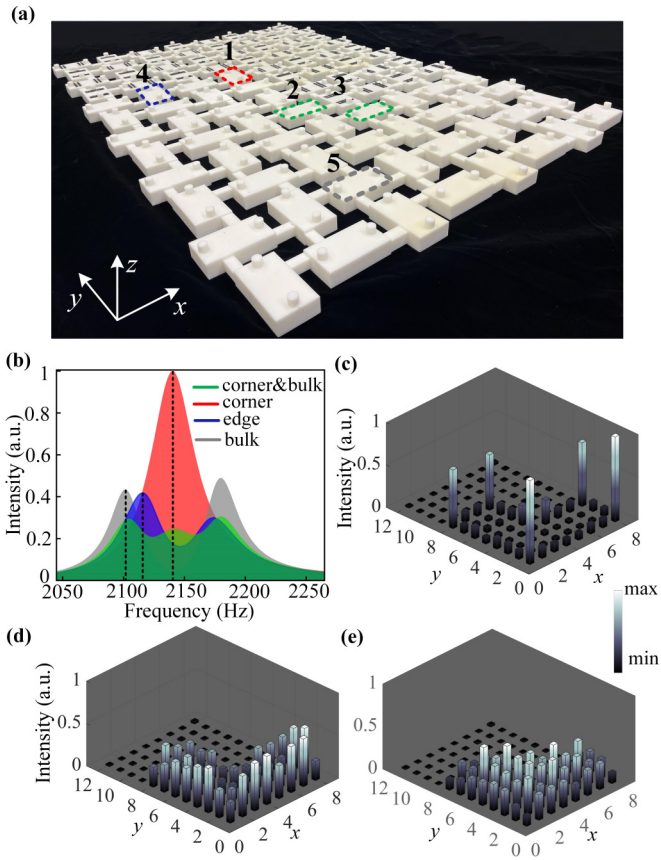

FIG. 4. Measured acoustic responses of the lattice with an L-shaped HLS. (a) Photo of the sample with 8×12 site cavities. (b) Measured spectra in cavities 1, 4, and 5 labeled in (a), respectively, corresponding to the bulk-evolved corner (in red), bulk-evolved edge (in blue), and bulk (in gray) modes. The green spectrum is measured in cavity 2, which is occupied by a bulk-evolved corner mode and two bulk modes. The spectrum in cavity 3 is similar to the green one. (c)–(e) Measured acoustic intensity profiles at 2141, 2114, and 2100 Hz, corresponding to frequencies denoted by the dotted black lines in (b). Both the color and height represent the intensity.

spectrum [the blue one in Fig. 3(b)] have a smaller interval, confirming the theoretical prediction in Fig. 2. By contrast, for the corner spectrum measured in the lowermost cavity of the interface [labeled as "1" in Fig. 3(a)], only one single peak at the midgap frequency of 2141 Hz is observed [depicted by the red plot in Fig. 3(b)]. By respectively exciting and measuring all the sites, the site-resolved acoustic intensity profiles at peak frequencies of the three spectra [denoted by the black dotted lines in Fig. 3(b)] are obtained and displayed in Figs. 3(c)–3(e), respectively. The energy profile at 2141 Hz in Fig. 3(c) demonstrates the emergence of eight corner localizations. Besides the original four corners, four energy concentrations appear at the interface corners. Moreover, the edge-mode profile [Fig. 3(d)] shows that the overall intensity along the edges and interfaces is higher than that in the interior, distinct from the bulk mode [Fig. 3(e)]. All the experimental results agree well with our full-wave simulations (see note S6 in Ref. [33]).

Non-Hermiticity facilitates the topological edge transport and corner localization with diverse patterns inside the lattice. To reveal such flexible reconfigurability, the rectangular pattern of the HLS is replaced by an "L" shape [Figs. 1(b) and 4(a)]. Surprisingly, in the inner bulk cavity [site 1 in Fig. 4(a)], only one peak appears in the measured spectrum [red area in Fig. 4(b)], similar to the one in Fig. 3(b). These results evidence that the bulk-evolved corner modes have almost the same characteristics as the edge-evolved ones as long as they exceed the corresponding EPs. The green spectrum in Fig. 4(b) depicts the intensity spectrum measured in cavity 2 (or cavity 3), which is located at the other turning corner within the lattice. Unlike before, three separated peaks are observed at 2103, 2141, and 2183 Hz, respectively, indicating that a midgap corner mode coexists with the gapped bulk modes in these two cavities. This response is evidenced by comparing the corner-mode profile in Fig. 1(d) and bulk-mode profile in Fig. S5(d) in Ref. [33], where the two blue dots outside the black dotted lines correspond to the cavities 2 and 3 in Fig. 4(a). The bulk and edge spectra measured in cavity 5 and cavity 4 are indicated by the gray and blue colors in Fig. 4(b), respectively, consistent with the measured results in Fig. 3(b), which further demonstrate their stability regardless of the subarea patterns. Similarly, we also measure the responses of the whole sample for the corner (2141 Hz), edge (2114 Hz), and bulk (2100 Hz) modes, as shown in Figs. 4(c)–4(e), respectively, which clearly demonstrate the energy localizations at the predicted corners and edges.

IV. CONCLUSION

We have experimentally demonstrated the manipulations of topological modes by constructing different types of non-Hermitian interfaces, both sides of which are applied with imbalanced losses. When the loss contrast is sufficiently large, both the first-order and higher-order TMs can be observed in the interfaces. By designing the interface patterns, the energy localization modes can be flexibly controlled. This non-Hermitian scheme is generally applicable to other classical wave systems, such as the elastic lattice consisting of resonant plates and connecting beams [24] and photonic lattices [12,39]. Besides, other types of TMs, for example, the higher-order topological defect modes in the honeycomb or hexagonal lattices [34,40–42] and third-order TMs in the three-dimensional octupole topological insulators [35] can also be flexibly modulated. By making further efforts to introduce active elements [43,44], the emergence of TMs can be switched dynamically, which is beneficial to push the topological devices towards practical applications.

ACKNOWLEDGMENTS

This work was supported by the Hong Kong Research Grants Council via General Research Funds (Grants No. 15200922, No. 15202820, and No. 15204419), and Hong Kong Innovation and Technology Commission via project "Smart Railway Technology and Applications" (Grant No. K-BBY1).

[1] H. Huang, J. Chen, and S. Huo, Recent advances in topological elastic metamaterials, J. Phys.: Condens. Matter. **33**, 503002 (2021).

[2] G. Ma, M. Xiao, and C. T. Chan, Topological phases in acoustic and mechanical systems, Nat. Rev. Phys. **1**, 281 (2019).

[3] T. Ozawa, H. M. Price, A. Amo, N. Goldman, M. Hafezi, L. Lu, M. C. Rechtsman, D. Schuster, J. Simon, O. Zilberberg, and I. Carusotto, Topological photonics, Rev. Mod. Phys. **91**, 015006 (2019).

[4] G. M. Graf and M. Porta, Bulk-edge correspondence for two-dimensional topological insulators, Commun. Math. Phys. **324**, 851 (2013).

[5] F. D. M. Haldane, Nobel lecture: Topological quantum matter, Rev. Mod. Phys. **89**, 040502 (2017).

[6] W. A. Benalcazar, B. A. Bernevig, and T. L. Hughes, Quantized electric multipole insulators, Science **357**, 61 (2017).

[7] W. A. Benalcazar, B. A. Bernevig, and T. L. Hughes, Electric multipole moments, topological multipole moment pumping, and chiral hinge states in crystalline insulators, Phys. Rev. B **96**, 245115 (2017).

[8] B. Xie, H.-X. Wang, X. Zhang, P. Zhan, J.-H. Jiang, M. Lu, and Y. Chen, Higher-order band topology, Nat. Rev. Phys. **3**, 520 (2021).

[9] M. Serra-Garcia, V. Peri, R. Susstrunk, O. R. Bilal, T. Larsen, L. G. Villanueva, and S. D. Huber, Observation of a phononic quadrupole topological insulator, Nature (London) **555**, 342 (2018).

[10] C. W. Peterson, W. A. Benalcazar, T. L. Hughes, and G. Bahl, A quantized microwave quadrupole insulator with topologically protected corner states, Nature (London) **555**, 346 (2018).

[11] S. Imhof, C. Berger, F. Bayer, J. Brehm, L. W. Molenkamp, T. Kiessling, F. Schindler, C. H. Lee, M. Greiter, T. Neupert, and R. Thomale, Topolectrical-circuit realization of topological corner modes, Nat. Phys. **14**, 925 (2018).

[12] S. Mittal, V. V. Orre, G. Zhu, M. A. Gorlach, A. Poddubny, and M. Hafezi, Photonic quadrupole topological phases, Nat. Photonics **13**, 692 (2019).

[13] Y. Qi, C. Qiu, M. Xiao, H. He, M. Ke, and Z. Liu, Acoustic Realization of Quadrupole Topological Insulators, Phys. Rev. Lett. **124**, 206601 (2020).

[14] Z.-G. Chen, C. Xu, R. Al Jahdali, J. Mei, and Y. Wu, Corner states in a second-order acoustic topological insulator as bound states in the continuum, Phys. Rev. B **100**, 075120 (2019).

[15] B. Y. Xie, G. X. Su, H. F. Wang, H. Su, X. P. Shen, P. Zhan, M. H. Lu, Z. L. Wang, and Y. F. Chen, Visualization of Higher-Order Topological Insulating Phases in Two-Dimensional Dielectric Photonic Crystals, Phys. Rev. Lett. **122**, 233903 (2019).

[16] X. Zhang, H.-X. Wang, Z.-K. Lin, Y. Tian, B. Xie, M.-H. Lu, Y.-F. Chen, and J.-H. Jiang, Second-order topology and multidimensional topological transitions in sonic crystals, Nat. Phys. **15**, 582 (2019).

[17] X. Ni, M. Weiner, A. Alu, and A. B. Khanikaev, Observation of higher-order topological acoustic states protected by generalized chiral symmetry, Nat. Mater. **18**, 113 (2019).

[18] C. Scheibner, W. T. M. Irvine, and V. Vitelli, Non-Hermitian Band Topology and Skin Modes in Active Elastic Media, Phys. Rev. Lett. **125**, 118001 (2020).

[19] T. Hofmann, T. Helbig, F. Schindler, N. Salgo, M. Brzezińska, M. Greiter, T. Kiessling, D. Wolf, A. Vollhardt, A. Kabaši, C. H. Lee, A. Bilušić, R. Thomale, and T. Neupert, Reciprocal skin effect and its realization in a topolectrical circuit, Phys. Rev. Res. **2**, 023265 (2020).

[20] S. Weidemann, M. Kremer, T. Helbig, T. Hofmann, A. Stegmaier, M. Greiter, R. Thomale, and A. Szameit, Topological funneling of light, Science **368**, 311 (2020).

[21] H. Gao, H. Xue, Q. Wang, Z. Gu, T. Liu, J. Zhu, and B. Zhang, Observation of topological edge states induced solely by non-Hermiticity in an acoustic crystal, Phys. Rev. B **101**, 180303(R) (2020).

[22] X. W. Luo and C. Zhang, Higher-Order Topological Corner States Induced by Gain and Loss, Phys. Rev. Lett. **123**, 073601 (2019).

[23] S. Liu, S. Ma, C. Yang, L. Zhang, W. Gao, Y. J. Xiang, T. J. Cui, and S. Zhang, Gain- and Loss-Induced Topological Insulating Phase in a Non-Hermitian Electrical Circuit, Phys. Rev. Appl. **13**, 014047 (2020).

[24] H. Fan, H. Gao, S. An, Z. Gu, S. Liang, Y. Zheng, and T. Liu, Hermitian and non-Hermitian topological edge states in one-dimensional perturbative elastic metamaterials, Mech. Syst. Signal Process. **169**, 108774 (2022).

[25] Z. Gu, H. Gao, P.-C. Cao, T. Liu, X.-F. Zhu, and J. Zhu, Controlling Sound in Non-Hermitian Acoustic Systems, Phys. Rev. Appl. **16**, 057001 (2021).

[26] K. Ding, G. Ma, M. Xiao, Z. Q. Zhang, and C. T. Chan, Emergence, Coalescence, and Topological Properties of Multiple Exceptional Points and Their Experimental Realization, Phys. Rev. X **6**, 021007 (2016).

[27] M. A. Miri and A. Alu, Exceptional points in optics and photonics, Science **363**, 42 (2019).

[28] B. Peng, Ş. K. Özdemir, S. Rotter, H. Yilmaz, M. Liertzer, F. Monifi, C. M. Bender, F. Nori, and L. Yang, Loss-induced suppression and revival of lasing, Science **346**, 328 (2014).

[29] Z. Lin, H. Ramezani, T. Eichelkraut, T. Kottos, H. Cao, and D. N. Christodoulides, Unidirectional Invisibility Induced by PT-Symmetric Periodic Structures, Phys. Rev. Lett. **106**, 213901 (2011).

[30] T. Liu, X. Zhu, F. Chen, S. Liang, and J. Zhu, Unidirectional Wave Vector Manipulation in Two-Dimensional Space with an All Passive Acoustic Parity-Time-Symmetric Metamaterials Crystal, Phys. Rev. Lett. **120**, 124502 (2018).

[31] H. Zhao, X. Qiao, T. Wu, B. Midya, S. Longhi, and L. Feng, Non-Hermitian topological light steering, Science **365**, 1163 (2019).

[32] Y. Li, C. Fan, X. Hu, Y. Ao, C. Lu, C. T. Chan, D. M. Kennes, and Q. Gong, Effective Hamiltonian for Photonic Topological Insulator with Non-Hermitian Domain Walls, Phys. Rev. Lett. **129**, 053903 (2022).

[33] See Supplemental Material at http://link.aps.org/supplemental/10.1103/PhysRevB.107.L201108 for more discussion of the exceptional points, the robustness of topological modes, the bulk quadrupole moment, the simulated field-intensity distribution, and the details for simulation and experiment, which include Ref. [45].

[34] H. Xue, Y. Yang, F. Gao, Y. Chong, and B. Zhang, Acoustic higher-order topological insulator on a kagome lattice, Nat. Mater. **18**, 108 (2019).

[35] H. Xue, Y. Ge, H. X. Sun, Q. Wang, D. Jia, Y. J. Guan, S. Q. Yuan, Y. Chong, and B. Zhang, Observation of an acoustic octupole topological insulator, Nat. Commun. **11**, 2442 (2020).

[36] H. Xue, D. Jia, Y. Ge, Y. J. Guan, Q. Wang, S. Q. Yuan, H. X. Sun, Y. D. Chong, and B. Zhang, Observation of Dislocation-Induced Topological Modes in a Three-Dimensional Acoustic Topological Insulator, Phys. Rev. Lett. **127**, 214301 (2021).

[37] T. Li, J. Du, Q. Zhang, Y. Li, X. Fan, F. Zhang, and C. Qiu, Acoustic Möbius Insulators from Projective Symmetry, Phys. Rev. Lett. **128**, 116803 (2022).

[38] H. Gao, H. Xue, Z. Gu, T. Liu, J. Zhu, and B. Zhang, Non-Hermitian route to higher-order topology in an acoustic crystal, Nat. Commun. **12**, 1888 (2021).

[39] M. Hafezi, S. Mittal, J. Fan, A. Migdall, and J. M. Taylor, Imaging topological edge states in silicon photonics, Nat. Photonics **7**, 1001 (2013).

[40] J. Noh, W. A. Benalcazar, S. Huang, M. J. Collins, K. P. Chen, T. L. Hughes, and M. C. Rechtsman, Topological protection of photonic mid-gap defect modes, Nat. Photonics **12**, 408 (2018).

[41] H. Fan, B. Xia, L. Tong, S. Zheng, and D. Yu, Elastic Higher-Order Topological Insulator with Topologically Protected Corner States, Phys. Rev. Lett. **122**, 204301 (2019).

[42] M. Li, D. Zhirihin, M. Gorlach, X. Ni, D. Filonov, A. Slobozhanyuk, A. Alù, and A. B. Khanikaev, Topological protection of photonic mid-gap defect modes, Nat. Photonics **14**, 89 (2019).

[43] J. J. Liu, Z. W. Li, Z. G. Chen, W. Tang, A. Chen, B. Liang, G. Ma, and J. C. Cheng, Experimental Realization of Weyl Exceptional Rings in a Synthetic Three-Dimensional Non-Hermitian Phononic Crystal, Phys. Rev. Lett. **129**, 084301 (2022).

[44] C. Shi, M. Dubois, Y. Chen, L. Cheng, H. Ramezani, Y. Wang, and X. Zhang, Accessing the exceptional points of parity-time symmetric acoustics, Nat. Commun. **7**, 11110 (2016).

[45] F. Zangeneh-Nejad and R. Fleury, Topological analog signal processing, Nat. Commun. **10**, 2058 (2019).